ELECTROMAGNETIC
METHODS

Simulation and Implementation of a High Sensitive Differential Eddy Current Giant Magnetoresistance Probe for Non-Destructive Testing

Dalal Radia Touil[a],*, Ahmed Chaouki Lahrech[a], Bachir Helifa[a], and Ibn Khaldoun Lefkaier[a]

[a] Materials Physics Laboratory, Amar Telidji University of Laghouat, Laghouat, 03000 Alegria
* e-mail: dtouil993@gmail.com

Abstract—This paper presents the design and implementation of a high-sensitivity eddy current (EC) sensor based on giant magnetoresistance (GMR) to assess cracks in conductive materials. This approach's originality uses two symmetrical giant magnetoresistance sensors in a differential configuration using commercial GMR elements inserted on a coil in a ferrite pot. The background signal measured by the sensor is infinitesimal if there is no crack in the sample. Therefore, the designed sensor demonstrates a high sensitivity to the presence of cracks where the GMRs mounted in differential allow to reduce the background voltage's impact. On the other hand, The GMR-based EC probe with a ferrite pot core is more sensitive to the presence of cracks than the conventional EC sensor without a ferrite pot core. This work introduces the notion of the GMR sensor's effective area (EA) after being calculated and optimized using the inverse problem (particle swarm optimization method). The operation of the differential GMR sensor is validated using a 3D finite element model based on the (A, V–A) formulation and experimental measurements. The prototype of the differential GMR sensor is developed and tested. Experimental results are obtained to evaluate cracks machined on an aluminum standard.

1. INTRODUCTION

The main role of non destructive testing (NDT) is to detect and evaluate the size of cracks in critical parts of industrial devices [1]. The current challenge lies in detecting of smaller and smaller defects while reducing the inspection time. Inductive sensors are the most commonly used in eddy current non-destructive testing (EC-NDT). Their high sensitivity in EC-NDT systems allows for improved performance in detecting deep cracks [2]. Nevertheless, low-frequency eddy current (ECT) controls require sensors with high field sensitivity and high spatial resolution [3].

In order to exceed the performance of wire wound sensors in sensitivity and resolution, we use giant magnetoresistance (GMR) [4–6], which are characterized by high sensitivity, low frequency making them suitable for many practical applications, including crack assessment [4–8], wide dynamic range, and are relatively easy to realize and cheap [9–11]. Which is suitable for many practical applications, including crack assessment [4–8].

GMR sensors in the field of NDT have triggered the development of very sensitive probes [11, 15]. For example, authors such as Ramírez-Pacheco [16], developed an experimental eddy current (EC) system to characterize near-side cracks in Aluminum by slightly moving the GMR sensor with respect to the center of the excitation coil. In [17], Romero-Arismendi analyzed the influence of design parameters on the sensitivity of the GMR-based sensor. Nevertheless, GMR sensors for NDT applications are still under development; mainly, in the mentioned work, the probe's sensitivity regarding its design parameters was not fully characterized. To address these constraints, a new sensor design is investigated.

First, the area of action of the commercial GMR sensor is evaluated using the inverse problem method that minimizes the difference between the calculated and measured magnetic field strength using the particle swarm optimization (PSO) algorithm. This work approach uses two symmetric giant magnetoresis-
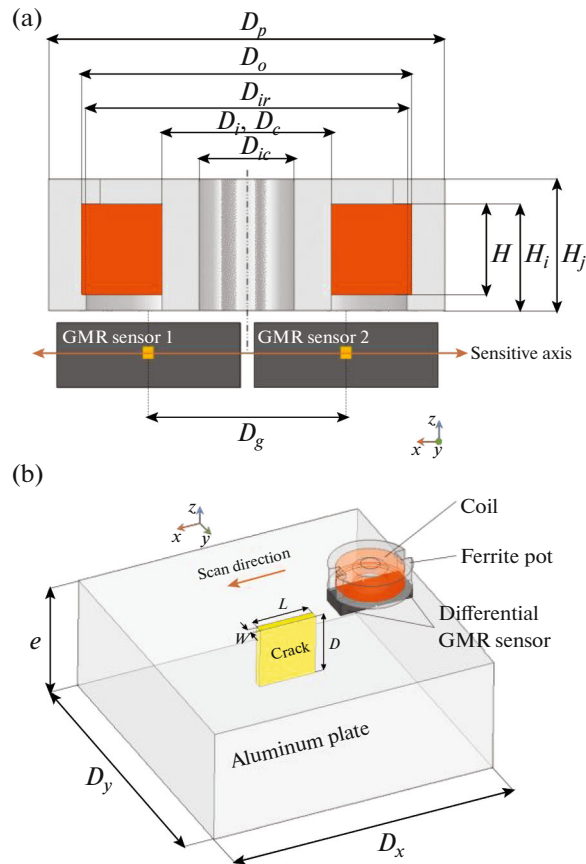
Fig. 1. Dimensions of the test sample and probe geometry.

tance sensors in a differential configuration using commercial GMR elements inserted on a ferrite pot coil.

The operation of the differential GMR sensor is validated throught a 3D finite element model (FEM) based on (A, V–A) formulation and experimental measurements. Finally, the development and realization of the differential GMR sensor prototype are established then the sensor is tested to evaluate cracks machined on an aluminum standard.

2. PROBE DESIGN

We focus carefully on choosing the characteristics of the excitation coil, according to our knowledge of AAH002-02 GMR sensor proprieties. The GMR-based eddy current probe's proposed concept is depicted in Fig. 1a. This probe is composed of a plane coil mounted on a ferrite pot core and two GMR sensors placed beneath the coil at a distance of 0.1 mm (lift-off) to operate in a differential configuration, i.e., the output of one sensor is subtracted from the output of the other one to obtain the probe output. GMR sensors are excited by a constant current source. The coil is excited by a sinusoidal current source whose frequency and amplitude can be adjusted. The magnetic field generated by the coil is sinusoidal in time, as are the eddy currents induced in the Aluminium sample, including the crack shown in Fig. 1b. Therefore, the output voltage is zero for a crack-free sample. If there is a crack in the sample, the crack will disturb the eddy current distribution. Since the background voltage is zero, the crack signal is abrupt to the output of the design probe.

3. DETERMINATION OF THE ACTIVE AREA OF THE GMR SENSOR

Since it is not possible to measure directly; the dimensions of the active area of the commercial GMR sensor, we evaluate the detectable area geometrical of the GMR used in the probe using the inverse prob-
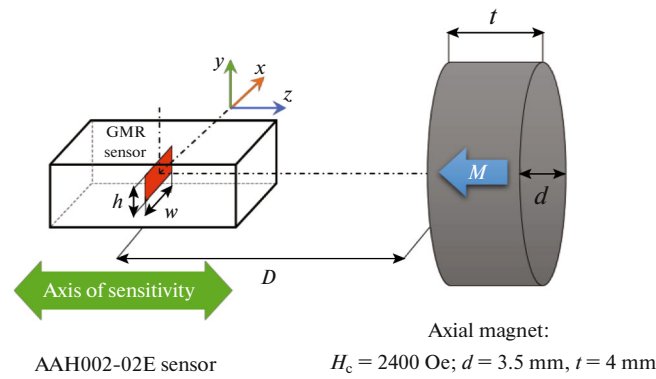
Fig. 2. Geometric model representing the parameters of the numerical model implemented for magnetic field strength calculations of permanent magnet as a function of distance (axial magnet).

lem method that consists of minimizing the difference between the computed and measured magnetic field strength at the GMR sensor's location.

The proposed magnetic field measurement method is a direct one (the GMR sensor acts as a magnetometer by measuring the magnetic field generated by the permanent magnet). Thus, magnetic field B will produce a change of the output voltage on the GMR sensor. Figure 2 illustrates the geometric and characteristic dimensions of the numerical model implemented for magnetic field strength calculations of the permanent magnet as a distance function (axial magnet). There are two principal parameters of the GMR sensor detectable area. The width w and the height h of the area. The inverse problem goal function is minimized using the particle swarm optimization (PSO) algorithm to evaluate the detectable area dimensions according to the measurement of the magnetic field strength at the GMR sensor's location.

A 3D finite element model was used to understand the physical principle and study the performance of the GMR sensor. The model was based on magnetic vector potential a formulation. The equation solved by the finite element method in a magneto static application is written as:

$$\nabla \times (v_0 v_r \nabla \times (\vec{A}) - \vec{H}_c) = 0, \tag{1}$$

where v_r is the relative reluctivity of the medium, v_0 is the magnetic reluctivity of the vacuum, $\vec{A}$ is the magnetic vector potential, and $\vec{H}_c$ is the coercive magnetic field (permanent magnets). Once the magnetic vector potential is $\vec{A}$ determined, the "amount" of magnetic field "flowing" through the surface of the GMR sensor, is expressed as given by Eq. (2):

$$B = \frac{\Phi_B}{S} = \frac{1}{S} \int \int_s \nabla \times (\vec{A}) \circ \hat{n} da, \tag{2}$$

where $\vec{A}$ is the magnetic vector potential, S is the surface area, $\hat{n}$ is the unit vector normal to the surface, and da is an infinitesimal area element. In the linear range of the sensor's response, we can express the output voltage as:

$$\Delta U = S_{\text{eff}} B, \tag{3}$$

where S_{eff} is the effective sensitivity, which depends on the sensor type and supply voltage.

The magnetic field strength of the permanent magnet is measured using an experimental setup (Fig. 3) based on a direct microcontroller interface. The magnetic field strength of the permanent magnet is calculated using a 3D FEM model and then compared with that measured until the convergence criterion of the cost function is satisfied, as represented in (4). The detectable area dimensions of the GMR sensor are then identified. The inverse problem algorithm (Fig. 4) describes these steps.

PSO algorithm is applied to minimize the inverse problem goal function to identify the detectable area dimensions of the GMR sensor. This algorithm is a heuristic search technique that optimizes a problem by iteratively trying to improve candidate solutions concerning a given objective measure of fitness.
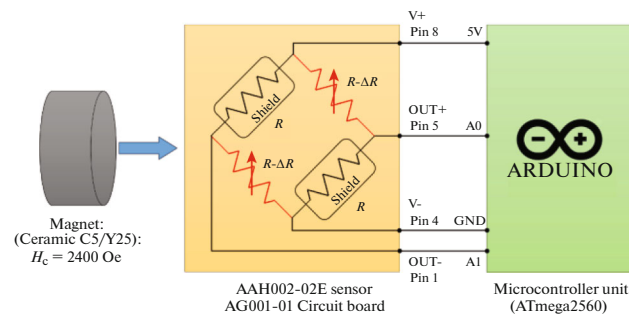
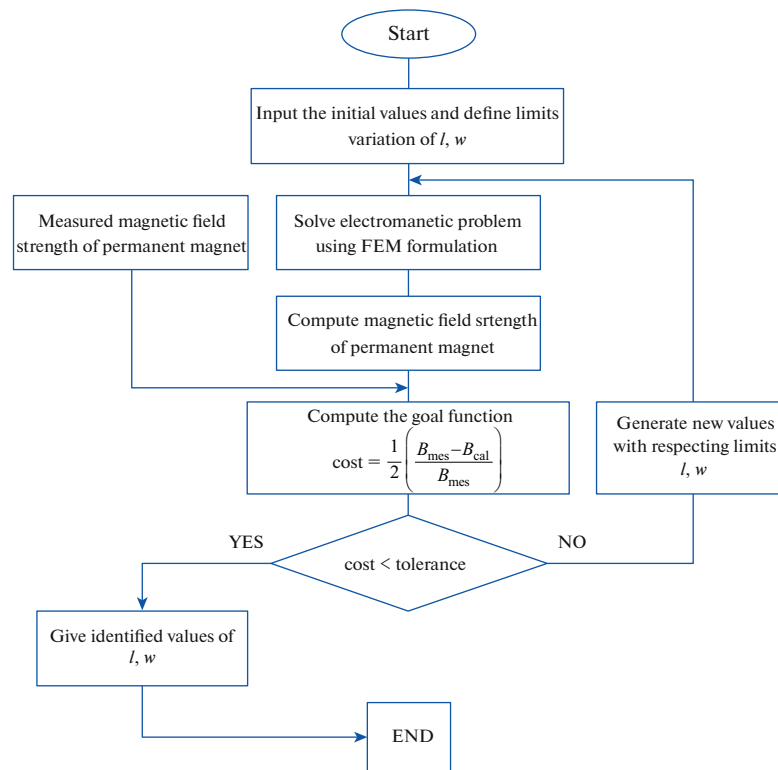**Fig. 3.** Schematic diagram of the experimental setup for magnetic field measurement using GMR sensor.

Fig. 4. Inverse problem algorithm.

The inverse problem goal function is written as:

$$\cos t = \frac{1}{2}\left(\frac{B_{\text{mes}} - B_{\text{cal}}}{B_{\text{mes}}}\right), \tag{4}$$

where B_{mes} and B_{cal}, respectively, is the measured and the computed magnetic field strength of the permanent magnet.

The obtained optimal detectable area dimensions of the GMR sensor, using inverse problem method at a distance value of 18 mm from face of the magnet to center of the AAH002-02E sensor package depicted in Fig. 5, are $w = 0.45$ mm and $h = 0.1$ mm.

These values of detectable area dimensions of the GMR sensor are introduced in the 3D model to compute the magnetic field strength of the permanent magnet as a function of distance. For an AAH002-02E GMR-based sensor, $S_m = 145$ mV/V/mT. At a supply voltage $V_s = 5$ V, one obtains $S_{\text{eff}} = 725$ mV/mT and an estimated output voltage $\Delta U_a = 210.25$ mV if $D = 18$ mm.
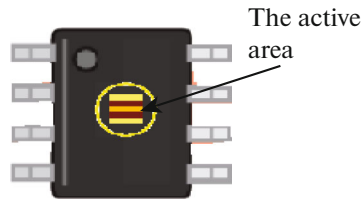
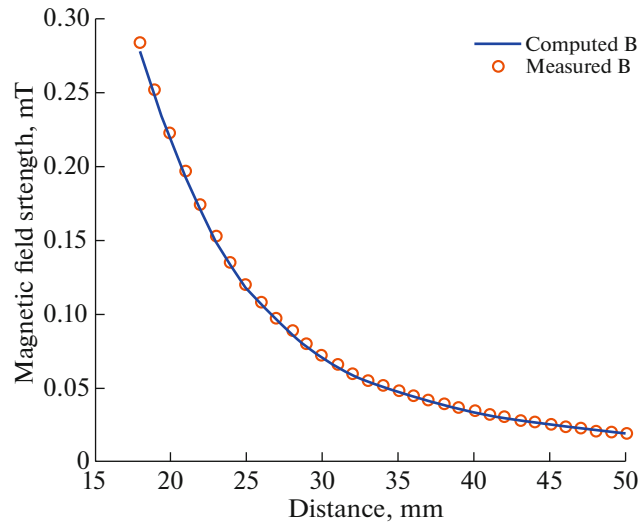**Fig. 5.** Position of the active area in the magnetometer proposed [19].

Fig. 6. 3D computed magnetic field strength of the permanent magnet and the measured one as a function of distance to identify the detectable area dimensions of the GMR sensor.

Figure 6 shows the comparison between the 3D computed magnetic field strength of the permanent magnet and the measured one. The experiment results validated the simulation.

4. MODEL-BASED PERFORMANCE STUDY

3D finite element method (FEM) model based on the A, V−A formulation is used to adjust the optimum position of the GMR sensor to have the maximum sensitivity point of the probe by slightly shifting the GMR sensor concerning the axis of the excitation coil.

4.1. D FEM Model

A 3D finite element model was developed to simulate the EC-GMR inspection system with a differential GMR sensor and study its performance. Moreover, to validate the operation of the differential sensor for detecting cracks in a multi-layer riveted structure. The formulation is based on magnetic vector and electric scalar potential; the gauged A, A−V formulation [18]. The magnetic vector potential is used in this formulation throughout the region, and the electric scalar potential only in, where, are, the eddy current free region (such as domains containing non-conducting media as well as coils with known current density), and the eddy current region. The partial differential equations of an eddy current field problem, having a unique solution according to Coulomb gauge, can be written as:

$$\nabla \times (v_0 \nabla \times A) - \nabla(v_0 \nabla \cdot A) + \sigma(i\omega A + \nabla V) = 0, \quad \text{in } \Omega_c, \tag{5}$$

$$\nabla \cdot (\sigma i\omega A + \sigma \nabla V) = 0, \quad \text{in } \Omega_c, \tag{6}$$

$$\nabla \times (v_0 v_r \nabla \times A) - \nabla(v_0 v_r \nabla \cdot A) = J_s, \quad \text{in } \Omega_n. \tag{7}$$
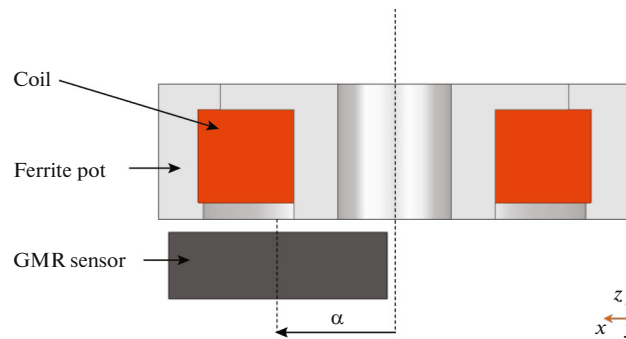
Fig. 7. Representation of the coil-GMR asymmetry value (α) in the GMR-based EC probe.

In (5) and (7), v_0 and v_r are, respectively, the reluctivity of vacuum and the relative reluctivity in the eddy current free region, σ is the electrical conductivity, ω is the angular frequency, and J_s is the source current density.

The GMR sensors operate in a differential configuration; the probe output is expressed as given by Eq. (8):

$$V_{\text{out}} = V_{\text{GMR},2} - V_{\text{GMR},1}. \tag{8}$$

Assuming that the two GMR sensors are operating within their linear range and considering $S_{\text{eff }1} = S_{\text{eff }2}$ (for the same type of sensors), the output voltage is proportional to the local magnetic field. Hence, the output of the differential probe can be expressed using Eq. (9):

$$V_{\text{out}} = S_{\text{eff}}(B_{\text{GMR},2} - B_{\text{GMR},1}), \tag{9}$$

where S_{eff} is the effective sensitivity (the sensor elements are carefully matched to ensure similar sensitivity levels), $B_{\text{GMR},1}$ and $B_{\text{GMR},2}$ are, respectively, the magnetic field flowing through the surface of the GMR1 sensor and the magnetic field flowing through the surface of the GMR2 sensor.

5. SIMULATION RESULTS

The simulation was performed in three steps:

In the first step, we studied adjusting the position of the GMR sensor to have the optimum sensitivity point of the probe. Therefore, we shifted the GMR sensor along the x-direction with a step of 0.01 mm. In Fig. 7, the symmetry axes of the coil and the sensor are shown, as well as the GMR-coil asymmetry (α). The curve begins with the symmetry position, the center of the excitation coil, proven by recent research such as Romero-Arismendi [17], which is the weakest sensitivity point. The results presented in Fig. 8 proved that 2.67 mm is the best position for the maximum output voltage of the GMR sensor, which shows the optimal sensitivity comparing with the centre value of the probe for best detection.

In the second step, after determining the optimal GMR sensor location, we studied the performance of the proposed differential GMR-based EC sensor. In this numerical example, we consider the system presented in Fig. 1. The numerical values of the modeled system parameters are given in Table 1.

The output voltages of the differential GMR-based eddy current sensor were studied based on the FEM model. Following four conditions were studied, particularly: (i) crack-free sample; (ii) sample with crack 1 (length = 1 mm, width = 1 mm, depth = 1 mm); (iii) sample with crack 3 (length = 3 mm, width = 3 mm, depth = 3 mm); and (iv) sample with crack 5 (length = 5 mm, width = 5 mm, depth = 5 mm). The GMR probe was moved along the y-axis from −10 to 10 mm with lift-off of 0.1 mm.

The amplitudes of the output of the differential-GMR probe are presented in Fig. 9. It is seen that the curve of the crack-free sample, that is, the red curve, is nearly zero, which confirms that the background signal measured in the crack-free area is null. Moreover, the output of the differential-GMR probe curves of three cracks (1, 3, and 5) show that the sensor is sensitive to cracks and confirmed that the amplitude increases with the depth of the crack to a particular value. After that, we justify the choice about the excitation coil by comparison between two symmetrical coils, one of them with ferrite pot core T6 in the same conditions of experience (the same current source passes through them); to test the influence of the ferrite pot core on the sensitivity of the GMR measurement probe, we simulate the same probe but with an excitation coil without a ferrite pot core, as illustrated in Fig. 10.
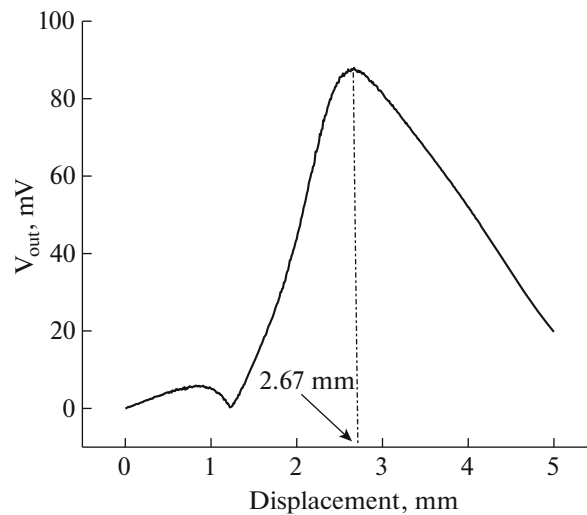
Fig. 8. Output voltage of the GMR sensor vs. GMR displacement along the coil radius is 5mm.
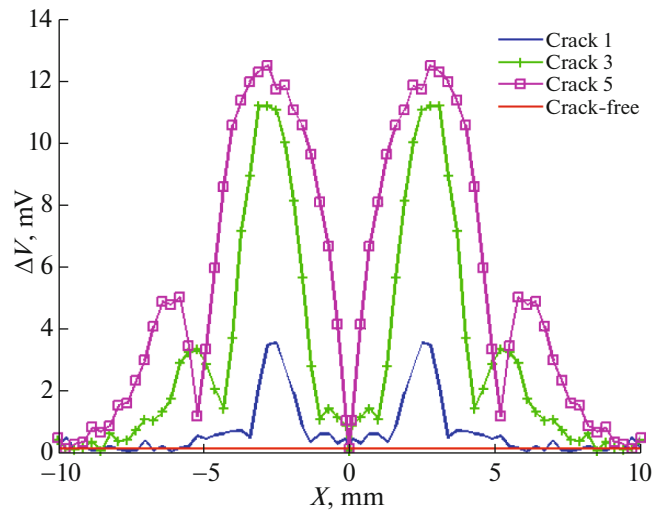

Fig. 9. Simulation result: output voltage of the differential probe vs. probe displacement for Four different conditions: crack 1; crack 3; crack 5, and crack-free.

The numerical results were compared in the same conditions, i.e., the excitation current was set at 8 mA amplitude at 10 kHz frequency, sample with crack are length × width × depth = 5 mm × 0.69 mm × 5 mm. The scan positions during the inspection were performed for 201 positions for the first probe and the second one.

Figure 11 shows the comparison between the results of the output voltage of the differential probe with a ferrite pot core as a function of displacement of the probe and the results of the output voltage of the differential probe without a ferrite pot core as a function of displacement of the probe. We notice that this ferrite pot core T6 of GMR-based EC probe adds 78.16% to the sensitivity to the presence of cracks than the conventional EC sensor without a ferrite pot core. We demonstrated that the magnetic field generated by the excitation ferrite core coil in the linear range of the transfer characteristic of the AAH002-02 GMR sensor used (0.06–0.3 mT). Then, the magnetic field generated by the excitation coil without ferrite core out the linear range of the GMR sensor.

To give an idea about the computing time in direct solutions. In the sample with crack 1 example, the probe coil, ferrite pot core, the standard AL-Alloy, the crack, and the air region are discretized respectively into 14 600, 14 800, 32 400, 35 600, and 71 600 elementary tetrahedrons. The resolution time on an

Table 1. Numerical values of the modeled system parameters

Element	Parameters	Values
Coil	Outer diameter (D_o)	9 mm
	Inner diameter (D_i)	4.7 mm
	Height (H)	2.2 mm
	Number of turns (N)	175
Ferrite pot core	Pot core outer diameter (D_p)	11 mm
	Core inner diameter (D_{ic})	
	Core diameter (D_c)	4.6 mm
	Crown inner diameter (D_{ir})	9.1 mm
	Inner height (H_i).	2.6 mm
	Core height (H_p)	3.2 mm
	Permeability (μ_r)	$4000 \pm 25\%$
Aluminum plate	Conductivity (σ)	19.63×10^6 S/m
	Thickness (e)	15 mm
	Surface ($D_x \times D_y$)	80×40 mm^2
Crack	Length (L)	1 mm
	Width (W)	0.69 mm
	Depth (D)	1 mm
GMR sensor	NVE AAH002-02	
	Distance between the GMR sensors (D_g)	5.34 mm
	Typical sensitivity	150 mV/V/mT
	Linear range	0.06−0.3 mT
	Saturation	0.6 mT
	Package	SOIC8
Power source	Intensity, frequency	8 mA, 10 kHz

Intel® Xeon ® CPU E5-2620 12-core Processor 2.00 GHz workstation with 128, GByte RAM is about 2 h and 30 min, which is reasonable considering the number of positions computed and the required precision.

6. EXPERIMENTAL IMPLEMENTATION

Section 4 presented simulation results that demonstrate the feasibility of the proposed probe. A prototype differential probe, data acquisition, and motion control system was developed and tested to demon-
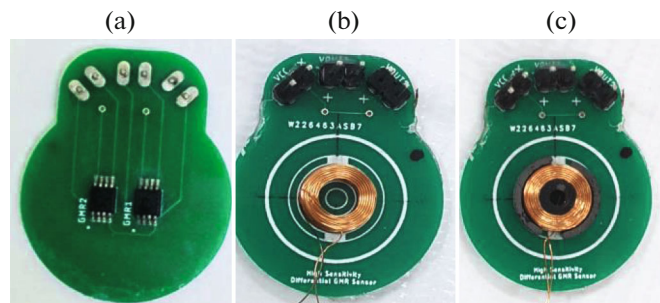

Fig. 10. Symmetrical coils: (a) up view probe with ferrite pot core; (b) up view probe without ferrite pot core; (c) down view of probes.
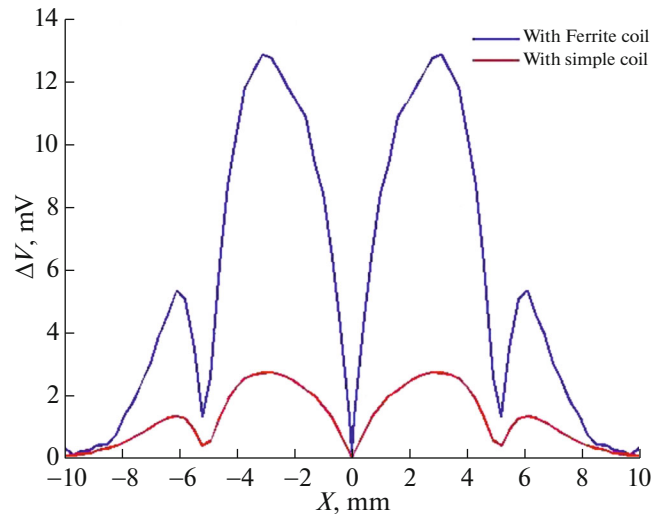
Fig. 11. Simulation result: comparison between the output voltage results by the differential probe with a ferrite pot core and the differential probe without a ferrite pot core.

strate the proof of concept. Figure 12 shows the experimental workbench used in this study. We used GMR sensor model AAH002-02E from nonvolatile electronics (NVE) to build the prototype probe. AAH002-02E is extremely sensitive to the magnetic field (typically 150 mV/V/mT) [19]. The measured range of the sensor is about 0.06−0.3 mT. The sensor can work in the frequency range from DC to 1 MHz. Moreover, we utilized two types of excitation coil, which SCIENSORIA Sarl supplied. The electrical characteristics of excitation coils measured at 10 kHz are reported in Table 2.

The aluminium standard was acquired from IZFP in Dresden, Germany. It is an aluminum alloy with machined slots of different sizes fabricated by laser devices μScan 6.5 according to the required shapes depicted in Fig. 13.

7. EXPERIMENTAL SETUP

The diagram of the experiment setup is shown in Fig. 14. The excitation signal was generated by a signal generator (GW INSTEK GFG-3015), which has one output channel. This signal generator was connected to the excitation coil via a coaxial cable, whose exciting frequency is set to 10 kHz. The AAH002-02E GMR sensors were supplied with a 1 V constant voltage of a lock-in amplifier auxiliary signal. For this voltage, the current through each sensor was about 0.5 mA (the internal resistance for each sensor is 2 kΩ ± 20%). A differential instrumentation amplifier is used to amplify the output signals from GMR sensors. Each channel was set to a gain of 10. The resulting signal is further amplified by another amplifier, which is set to a gain of 20. Considering the GMR sensors used are "omnipolar," meaning the output is equally sensitive to either magnetic field polarity, and the output is always a positive voltage which means that the differential output signal of the GMR sensor is a full-wave signal of 20 kHz frequency. The resulting signals are then connected to the lock-in amplifier's inputs ($V_{gmr1, in}$ and $V_{gmr2, in}$) multiplied by the reference signal (V_{ref}) at the same frequency, which the internal reference frequency was defined as

Table 2. Numerical values of electrical characteristics of a coil measured at 10 kHz

Parameters	Ferrite pot core coil	Simple coil
Voltage (V)	0.4386 V	0.09684 V
Current (I)	8 mA	8 mA
Impedance (Z)	54.5968 Ω	12.112 Ω
Magnetic field (B)	0.3 mT	0.07 mT
Output voltage of GMR sensor 1 and 2[a]	45 mV	10.1766 mV

[a] AAH002-02: linear range (22.5−45 mV) = (0.15−0.3 mT).
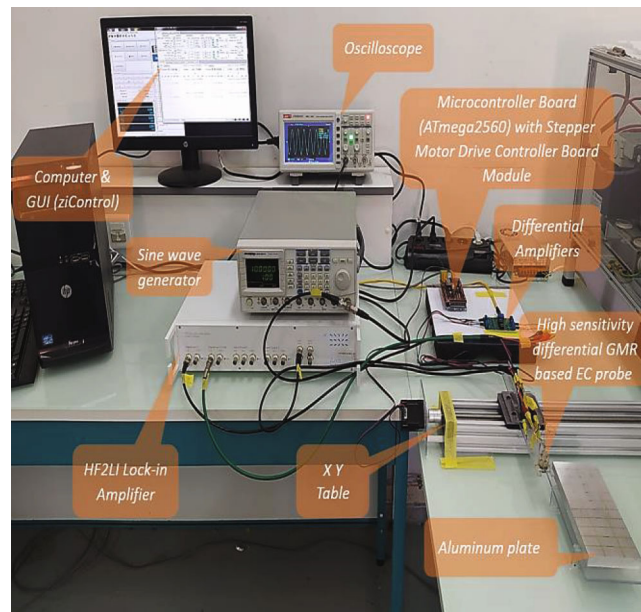
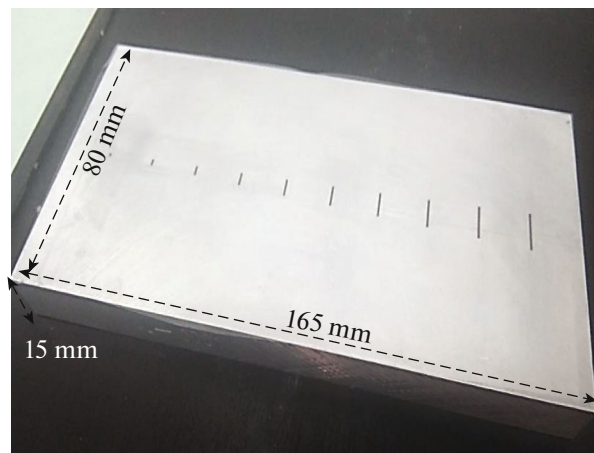**Fig. 12.** Picture of the experiment workbench.

Fig. 13. Standard aluminum alloy with machined flaws.

$f_{\text{eff}} = 2 \times 10$ kHz. The resulting signal has a DC offset and a frequency component at twice the frequency of $V_{\text{gmr1, in}}$ and V_{ref}. Since two almost identical AAH002-02E GMR sensors were used, a double differential measurement system where the advantages and precision compared with a single differential measurement setup was further amplified.

A personal computer (PC) was used as the central data acquisition controller. It communicated with an arduino microcontroller unit (AMU) through a USB cable. The AMU generated a driving signal for a step motor, which drives the probe to move on top of the tested aluminium standard. The HF2LI lock-in amplifier is used to obtain the baseband signals. The HF2LI lock-in amplifier outputs are sampled by 14 bits, 210 MSa/s analog to digital converter (ADC), and acquired by the computer through a USB cable.

The SNR of the experiment results was calculated according to the equation:

$$\text{SNR} = \frac{A_{\text{signal}}}{\sigma_{\text{noise}}} = \frac{12.4 \text{ mV}}{0.15 \text{ mV}} = 20 \log(83.33) = 38.34 \text{ dB}.$$
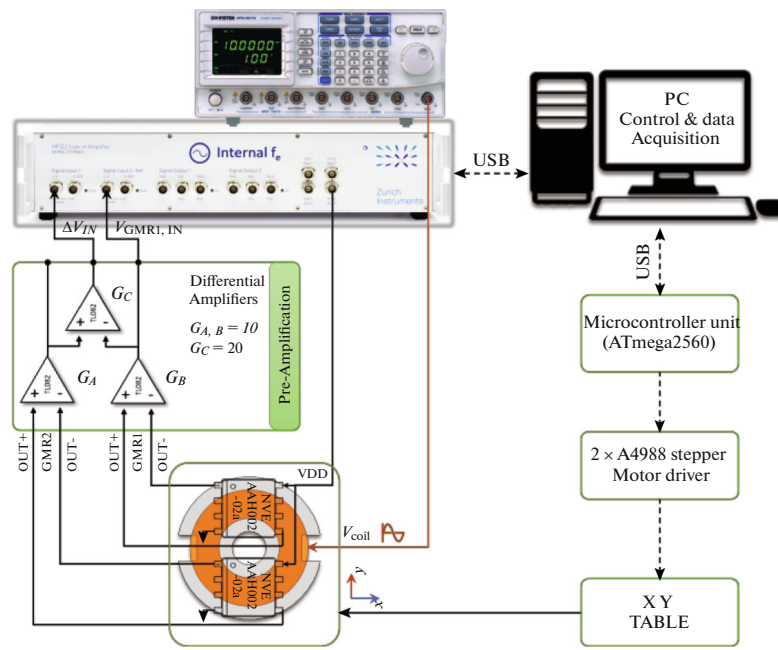
Fig. 14. Schematic diagram of the experimental setup.

8. EXPERIMENTAL RESULTS AND VALIDATION

The performance of the proposed differential probe for inspection of flaws in the aluminum sample was tested experimentally. The probe was moved along the x scan direction with a displacement step of 0.1 mm.

The excitation current was set at 8 mA amplitude at 10 kHz frequency. The aluminum standard from IKTS is an Al-0001 alloy. Its conductivity is 19.63×10^6 S/m. The dimensions of the rectangular Al standard are length × width × thickness = 165 mm × 80 mm × 15 mm. The dimensions of the machined flaws (length × width × depth) are shown in Table 3.

Figure 15 illustrates the experimental measurements of the output voltage of the differential probe as a function of displacement of the probe along the length for the first five flaws (1, 2, 3, 4, and 5). One can confirm that the EC signal strongly depends for thin flaws.

Figure 16 shows the experimental measurements of the output voltage of the differential probe as a function of displacement of the probe along the length for the second five flaws (6, 7, 8, 9, and 10). We notice that the signal amplitudes of the output voltages of the differential probe decreases whereas the flaws length and depth increase.

Table 3. Numerical values of dimensions of the cracks

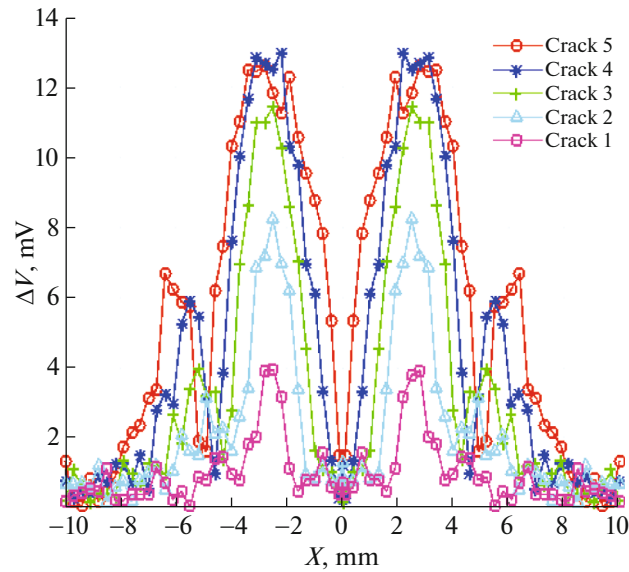| Cracks	Length, mm	Width, mm	Depth, mm
1	1.00	0.67	1.00
2	2.00	0.68	2.00
3	3.04	0.68	3.00
4	4.03	0.69	4.00
5	4.95	0.65	5.00
6	5.43	0.62	6.00
7	6.05	0.57	7.00
8	7.65	0.47	8.00
9	8.18	0.61	9.00
10	8.94	0.55	10.00

Fig. 15. Output voltage of the differential probe vs. probe displacement for cracks (1, 2, 3, 4, 5).
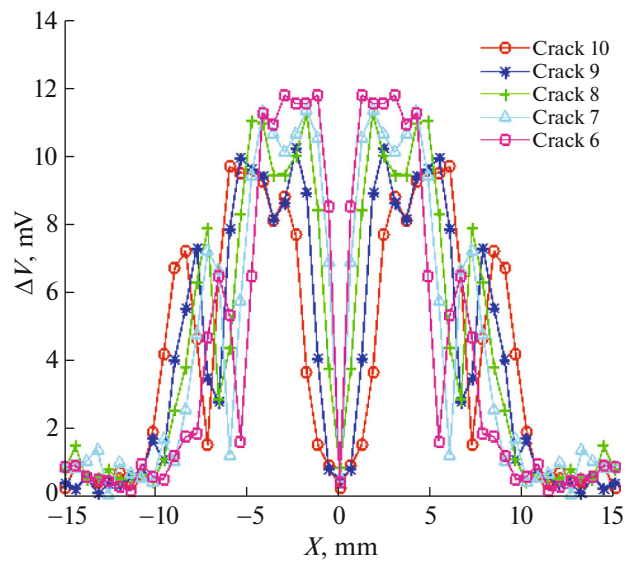

Fig. 16. Output voltage of the differential probe vs. probe displacement for cracks (6, 7, 8, 9, and 10).

We must note here that this phenomenon is not related to skin depth but is related with the distance between the two GMR sensors.

To check the validity of all systems, we compared the calculated and measured values of the output voltage of the differential GMR-based EC probe for a frequency of 10 kHz. Figure 17 shows a comparison between the computed output voltage of the du probe as a function of probe displacement and the measured ones in the case of the sample with flaw 5 (the same result was found for the other flaws of different sizes). We can notice that the two results are generally in good agreement.

The experiment results demonstrate the utility of the probe to detect cracks in materials while offering the advantages of high sensitivity and reliability.
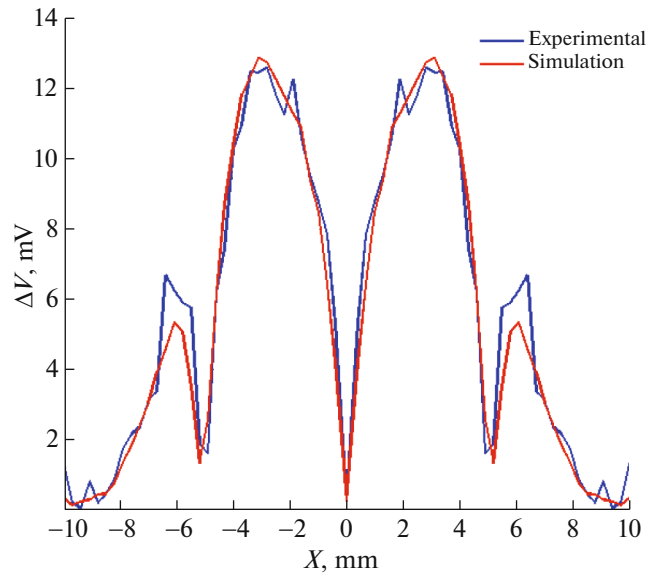
Fig. 17. Measured and output computed voltage of the dual probe vs. probe displacement in the case of the sample with flaw 5.

9. CONCLUSIONS

This paper presents the design and implementation of a high-sensitivity EC sensor based on GMR for inspecting aluminium samples with machined cracks. A significant contribution of this paper is to show that one can employ differential measurements from asymmetric differential GMR sensors to eliminate the background signal. Consequently, we conclude that the sensor has a much higher sensitivity to cracks than conventional EC sensors. The background signal of the GMR-based EC sensor measured on top of the crack-free sample is about 150 μV, which is 24 times smaller than the crack signal with dimensions 1 mm × 0.69 mm × 1 mm. The sensor has high relative sensitivity to the presence of a crack. It has also been demonstrated that the ferrite pot core T6 adds 78.16% to the sensitivity to the presence of cracks than the conventional EC sensor without a ferrite pot core. The differential probe's operation principle and crack signals were simulated using a 3D FEM model. A prototype unit was built and tested to demonstrate the proof of concept. The prototype probe scanned an aluminum sample with machined cracks. The experiment results validated the simulation model and established the utility of the probe to detect cracks in conductive materials while offering the advantages of high sensitivity and more excellent reliability, making it very attractive and reliable.

CONFLICT OF INTEREST

The authors declare that they have no conflicts of interest.

REFERENCES

1. Helifa, B., Oulhadj, A., Benbelghit, A., Lefkaier, I.K., Boubenider, F., and Boutassouna, D., Detection and measurement of surface cracks in ferromagnetic materials using eddy current testing, *NDT & E Int.,* 2006, vol. 39, no. 5, pp. 384–390.
https://doi.org/10.1016/j.ndteint.2005.11.004

2. Hamia, R., Cordier, C., and Dolabdjian, C., Separability of multiple deep crack defects with an NDE eddy current system, *IEEE Trans. Magn.,* 2013, vol. 49, no. 1, pp. 124–127.
https://doi.org/10.1109/TMAG.2012.2218796

3. Hamia, R., Cordier, C., Saez, S., and Dolabdjian, C., Eddy-current nondestructive testing using an improved GMR magnetometer and a single wire as inducer: A FEM performance analysis, *IEEE Trans. Magn.,* 2010, vol. 46, no. 10, pp. 3731–3737.
https://doi.org/10.1109/TMAG.2010.2052827

4. Rifai, D., Abdalla, A., Ali, K., and Razali, R., Giant magnetoresistance sensors: A review on structures and non-destructive eddy current testing applications, *Sensors,* 2016, vol. 16, no. 3, p. 298.
https://doi.org/10.3390/s16030298

5. Postolache, O., Ribeiro, A.L., and Ramos, H.G., GMR array uniform eddy current probe for defect detection in conductive specimens, *Measurement,* 2013, vol. 46, no. 10, pp. 4369−4378.
https://doi.org/10.1016/j.measurement.2013.06.050

6. Bernieri, A., Ferrigno, L., Laracca, M., and Rasile, A., Eddy current testing probe based on double-coil excitation and GMR sensor, *IEEE Trans. Instrum. Meas.,* 2019, vol. 68, no. 5, pp. 1533−1542.
https://doi.org/10.1109/TIM.2018.2890757

7. Kim, J., Yang, G., Udpa, L., and Udpa, S., Classification of pulsed eddy current GMR data on aircraft structures, *NDT & E Int.,* 2010, vol. 43, no. 2, pp. 141−144.
https://doi.org/10.1016/j.ndteint.2009.10.003

8. Smith, C.H., Eddy-current testing with GMR magnetic sensor arrays, *AIP Conf. Proc.* (Green Bay, Wisconsin (USA), 2004), vol. 700, pp. 406−413.
https://doi.org/10.1063/1.1711651

9. Zorni, C., Contrôle non destructif par courants de Foucault de milieux ferromagnétiques: de l'expérience au modèle d'interaction, p. 120.

10. Reimund, V., Pelkner, M., Kreutzbruck, M., and Haueisen, J., Sensitivity analysis of the non-destructive evaluation_of micro-cracks using GMR sensors, *NDT & E Int.,* 2014, vol. 64, pp. 21−29.
https://doi.org/10.1016/j.ndteint.2014.02.003

11. Dogaru, T. and Smith, S.T., Giant magnetoresistance-based eddy-current sensor, *IEEE Trans. Magn.,* 2001, vol. 37, no. 5, pp. 3831−3838.
https://doi.org/10.1109/20.952754

12. Yin, W. et al., Custom edge-element FEM solver and its application to eddy-current simulation of realistic 2M-element human brain phantom: Applications of a custom FEM solver, *Bioelectromagnetics,* 2018, vol. 39, no. 8, pp. 604−616.
https://doi.org/10.1002/bem.22148

13. Yin, W. et al., An equivalent-effect phenomenon in eddy current non-destructive testing of thin structures, *IEEE Access,* 2019, vol. 7, pp. 70296−70307.
https://doi.org/10.1109/ACCESS.2019.2916980

14. Lu, M., Peyton, A., and Yin, W., Acceleration of frequency sweeping in eddy-current computation, *IEEE Trans. Magn.,* 2017, vol. 53, no. 7, pp. 1−8.
https://doi.org/10.1109/TMAG.2017.2688326

15. Gao, P., Wang, X., Han, D., and Zhang, Q., Eddy current testing for weld defects with different directions of excitation field of rectangular coil, in *2018 4th Int. Conf. Control Autom. Robotics (ICCAR)* (Auckland, April 2018), pp. 486−491.
https://doi.org/10.1109/ICCAR.2018.8384725

16. Ramirez-Pacheco, E.J., Espina-Hernandez, H., Caleyo, F., and Hallen, J.M., Defect detection in aluminium with an eddy currents sensor, in *2010 IEEE Electron. Robotics Automotive Mech. Conf.* (Cuernavaca, Mexico, September 2010), pp. 765−770.
https://doi.org/10.1109/CERMA.2010.91

17. Romero-Arismendi, N.O., Pérez-Benítez, J.A., Ramírez-Pacheco, E., and Espina-Hernández, J.H., Design method for a GMR-based eddy current sensor with optimal sensitivity, *Sens. Actuators, A*, 2020, vol. 314, p. 112348.
https://doi.org/10.1016/j.sna.2020.112348

18. Helifa, B., Féliachi, M., Lefkaier, I.K., Boubenider, F., Zaoui, A., and Lagraa, N., Characterization of surface cracks using eddy current NDT simulation by 3D-FEM and inversion by neural network, *Mater. Sci.,* 2016, vol. 31, no. 2, p. 9.

19. Available online at https://www.nve.com/Downloads/catalog.pdf. Accessed January 4, 2021.